

Supplementary Information

CeO₂ supported high-valence Fe oxide for highly active and stable water oxidation

¹Guangdong Provincial Key Lab of Nano-Micro Material Research, School of Chemical Biology and Biotechnology, Shenzhen Graduate School, Peking University, Shenzhen, China

²Shenzhen International Graduate School, Tsinghua University, Shenzhen, China

³College of Chemistry and Environmental Engineering, Shenzhen University, Shenzhen, China

⁴Institute of Engineering Innovation, The University of Tokyo, Tokyo, Japan

⁵Department of Applied Biology and Chemical Technology, The Hong Kong Polytechnic University, Hung Hom, Kowloon, Hong Kong SAR, China

⁶Department of Chemistry and Biochemistry, Northern Illinois University, DeKalb, Illinois 60115, USA

⁷School of Engineering, The University of Tokyo, 7-3-1 Hongo, Bunkyo-ku, Tokyo 113-8656, Japan

⁸Institute of Biomedical Engineering, Shenzhen Bay Laboratory, Shenzhen 518107, China

⁹These authors contributed equally: Hongzhi Liu, Jun Yu, Jinghuang Lin

*e-mail: yu.jun@pku.edu.cn; bhuang@polyu.edu.hk; chsyang@pku.edu.cn

Experiment methods

Materials

All the chemicals used in the experiments were analytical grade (AR) without additional purification. Cerium nitrate hexahydrate ($\text{Ce}(\text{NO}_3)_3 \cdot 6\text{H}_2\text{O}$, 99.5%, Aladdin), Iron nitrate nonahydrate ($\text{Fe}(\text{NO}_3)_3 \cdot 9\text{H}_2\text{O}$, 99%, Sinopharm). Ethanol ($\text{CH}_3\text{CH}_2\text{OH}$, 95%, Aladdin).

Cleaning of nickel foam

The purchased commercial nickel foam was sonically washed for ten minutes by sequential industrial alcohol, ultrapure water, dilute hydrochloric acid (37% concentrated hydrochloric acid and ultrapure water are mixed evenly in a ratio of one to ten), ultrapure water, and industrial alcohol.

Synthesis of $\text{CeO}_2@\text{NF}$, $\text{Fe}^{\text{HV}}/\text{CeO}_2@\text{NF}$, $\text{LFe}/\text{CeO}_2@\text{NF}$ and $\text{Fe}@\text{NF}$

For $\text{CeO}_2@\text{NF}$ catalyst, a cerium precursor solution (0.25 Mmol Ce^{3+} and 10 Mmol NaCl) was prepared by dissolving $\text{Ce}(\text{NO}_3)_3 \cdot 6\text{H}_2\text{O}$ (99.99%, Aldrich) and NaCl in deionized water (about 50 mL) and was heated to 70°C by the water bath. In the three-electrode system, NF of the working electrode (WE) in 70°C electroplating solution was applied with $-0.25 \text{ mA}/\text{cm}^2$ current density for 10 min to form homogeneous CeO_2 plating on the surface of NF. In this way, $\text{CeO}_2@\text{NF}$ catalyst was prepared.

For $\text{Fe}^{\text{HV}}/\text{CeO}_2@\text{NF}$ catalyst, immerse $\text{CeO}_2@\text{NF}$ precursor in ferric nitrate solution (50 mL, 0.5 M) for 90 min and then dry in the air (70°C) for a few minutes to obtain $\text{Fe}^{\text{HV}}/\text{CeO}_2@\text{NF}$ catalyst. The detailed formation mechanism of FeO_x nanoparticles in $\text{Fe}^{\text{HV}}/\text{CeO}_2@\text{NF}$ is as follows. Fe^{3+} was hydrolyzed and formed iron hydroxide, and the corresponding H^+ etched CeO_2 with the formation of defects. The defects can anchor the iron hydroxide nanoparticles. During the following annealing process in air, the iron hydroxide nanoparticles transformed into FeO_x nanoparticles.

For $\text{LFe}/\text{CeO}_2@\text{NF}$ catalyst, immerse $\text{CeO}_2@\text{NF}$ catalyst in ferric nitrate solution (50 mL, 0.6 M) for 90 min and then dry in the air (70°C) for a few minutes to obtain $\text{LFe}/\text{CeO}_2@\text{NF}$ catalyst.

For $\text{Fe}@\text{NF}$ catalyst, directly immerse cleaned NF in ferric nitrate solution (50 mL, 0.5 M) for 90 min and then dry in the air (70°C) for a few minutes to obtain $\text{Fe}@\text{NF}$ catalyst.

Characterization

Scanning electron microscopy (SEM) measurements were performed on the field emission SEM (ZEISS SUPRA® 55). X-ray photoelectron spectroscopy (XPS) studies were conducted on ESCALAB 250Xi (Thermo Fisher). The spectra were analyzed using XPSPEAK software and bound energy calibration was performed using C1s peaks of exotic hydrocarbons at 284.8 eV. Transmission electron microscopy (TEM), high resolution TEM (HR-TEM) and scanning (S)TEM-EDS images were measured with a JEOL JEM-3200FS. HAADF STEM images were characterized by STEM (JEM-ARM200 cold, JEOL Co. Ltd) operated at 200 keV. The HAADF STEM images were obtained with a detection angle of 90-200 mrad. STEM-EELS were recorded using an Enfinium spectrometer (Gatan Inc.) with an energy dispersion of 0.25 eV/channel. The samples were prepared by sonication the catalysts off from the nickel foam, then the suspensions with catalyst were dropped onto the copper grid. The element content of the sample was measured using an inductively coupled plasma emission spectrometer (ICP-AES, Arcos II MV). The XAFS data were collected on the Beamline 20-BM facility of the Advanced Photon Source (APS) at Argonne National Laboratory (ANL). Energies were selected using a double-crystal Si (111) monochromator while the detection I_0 and I_T used standard ionization chambers. To calibrate the energy, a reference Fe metal foil was used, which was measured in line with the samples. All XAFS measurements were carried out at room temperature in transmission mode with continuous scanning between 6915 and 7800 eV and a commercial Fe_2O_3 was also measured as a reference to estimate the valence state of Fe. The ^{57}Fe Mössbauer spectrum was recorded on an SEE Co W304 Mössbauer spectrometer, using a $^{57}\text{Co}/\text{Rh}$ source in transmission geometry. The data were fitted by using the MossWinn 4.0 software. The Fe-L soft X-ray absorption spectra were performed at the Beamlines MCD-A and MCD-B (Soochow Beamline for Energy Materials) in NSRL, which were measured in the total electron yield mode in a vacuum chamber ($<5 \times 10^{-8}$ Pa).

Electrochemical Measurements

A standard three-electrode system with 1 M KOH (pH=13.6) was used in the electrochemical tests by the CHI760E electrochemistry workstation, with a Hg/HgO

electrode and a Pt wire as the reference and counter electrodes, respectively. The scan rates were 10 mV/s for the linear sweep voltammetry tests. The measure frequency for EIS was 10^{-1} to 10^5 Hz. The 0.53 V vs Hg/HgO was applied in the Tafel slope test. The working electrodes were CeO₂@NF, Fe^{HV}/CeO₂@NF, LFe/CeO₂@NF and Fe@NF catalysts. The potentials were calibrated against the RHE according to the following equation: $E_{\text{RHE}} = E_{\text{Hg/HgO}} + 0.059 \text{ pH} + E^0_{\text{Hg/HgO}}$ ($E^0_{\text{Hg/HgO}} = 0.098\text{V}$, $\text{pH}=13.6$). In addition, the Ag/AgCl reference electrodes were used to prepare cerium dioxide precursor. The O₂ products were quantitatively analyzed by gas chromatography (GC, SHIMADZU GC-2014). The reactor was connected with an online GC with a mass flowmeter at the outlet line. This flowmeter could precisely measure the rate of the gas flow from the reactor into the GC. The reading rate was used to calculate the faradaic efficiencies of O₂ products. The faradaic efficiency was calculated according to the following equation.

$$\text{FE} = \frac{Q_g}{Q_t} = \frac{z n f}{Q t} = \frac{z f P \alpha v}{106 I R T}$$

where Q_g and Q_t are the charge transferred to O₂ and the total charge across the catalysts, respectively; z is the number of electrons required for one molecule product, and z is 4 for O₂; f is the faraday constant of 96485C/mol; P is the atmospheric pressure of 101325 Pa; α (parts per million) is the O₂ concentrations measured by GC; v (standard-state cubic centimeter per minute) is the gas flow rate displayed on the mass flowmeter between the GC and the reactor; I is the total current, R is the gas constant of 8.314 J/(mol·K); T is the room temperature of 298.15K. The Tafel plots of the overpotential vs. $\log(j)$ were recorded as described in the report (Nat Commun 2019, 10, 3899), and the linear portions at low overpotential were fitted to the Tafel equation ($\eta = a + b \log j$, where η is the overpotential, j is the cathodic current density, and b is the Tafel slope).

DFT Calculation Setup

To clarify the electronic modulations of Fe/CeO₂ and its contributions to the OER performance, we have applied the DFT calculations through the CASTEP packages in this work.¹ For all the calculations, the generalized gradient approximation (GGA) and Perdew-Burke-Ernzerhof (PBE) are utilized to provide accurate descriptions for the

exchange-correlation interactions in the structure.²⁻⁴ Meanwhile, we have selected the ultrasoft pseudopotentials for all the geometry optimizations and the plane-wave basis cutoff energy has been accordingly set to 380 eV. In particular, we choose the Broyden-Fletcher-Goldfarb-Shannon (BFGS) algorithm to reach efficient energy minimizations.⁵ Considering the balance between calculation efficiency and accuracy, we choose the coarse quality of k -points for the geometry optimizations. Fe/CeO₂ has been constructed based on the (111) surfaces of the CeO₂ with four-layer thickness, where abundant oxygen vacancies have been created on the surface. The ultra-small FeO_{*x*} nanoparticles have been constructed based on the FeO₂ structures to match the high valence states confirmed by experiments. The stringent convergence criteria have been set to guarantee accurate calculations as follows. (1) Hellmann-Feynman forces should not exceed 0.001 eV/Å; (2) the total energy difference should be less than 5×10^{-5} eV/atom, and (3) the inter-ionic displacement should be smaller than 0.005 Å.

Figures

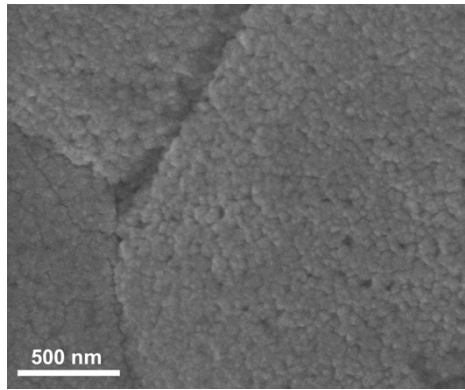


Fig. S1 SEM morphology of CeO₂@NF sample. A uniform electroplated layer, consisted of CeO₂ nanoparticles, is formed on the surface of NF.

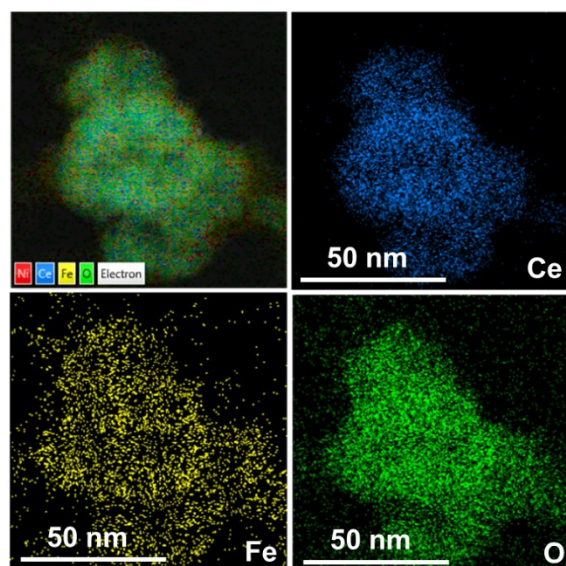


Fig. S2 STEM-EDS mapping image of $\text{Fe}^{\text{HV}}/\text{CeO}_2@\text{NF}$ catalyst. The STEM-EDS mapping images prove the uniform distribution of Ce and Fe in $\text{Fe}^{\text{HV}}/\text{CeO}_2@\text{NF}$.

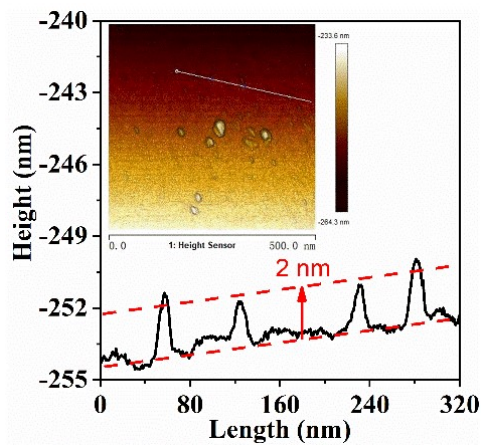


Fig. S3 AFM (atomic force microscope) image of FeO_x nanoparticles in $\text{Fe}^{\text{HV}}/\text{CeO}_2@\text{NF}$, showing the sizes of the FeO_x nanoparticles to be about 2 nm.

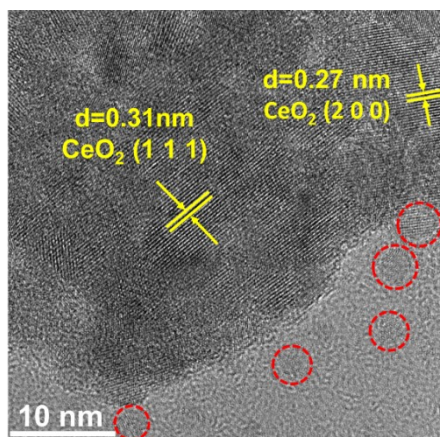


Fig. S4 HRTEM image of Fe^{HV}/CeO₂@NF.

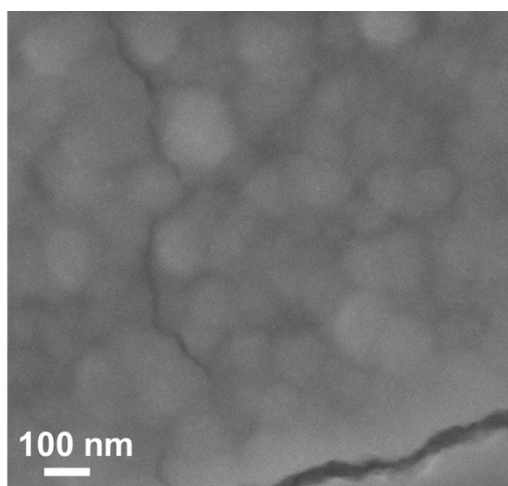


Fig. S5 SEM image of LFe/CeO₂@NF catalyst. The morphology of the LFe/CeO₂@NF catalyst presents larger iron oxide particles (~100 nm).

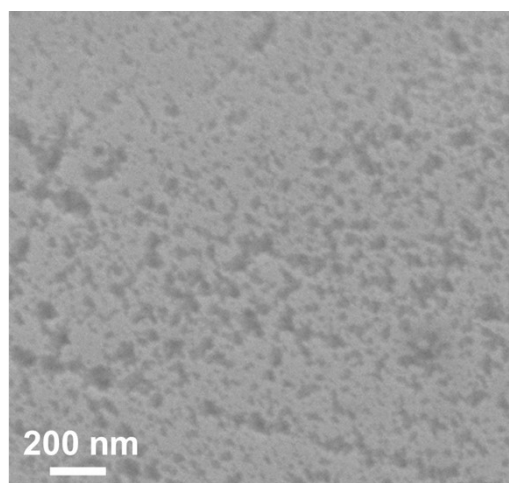


Fig. S6 SEM image of the Fe@NF catalyst. NF instead of CeO₂@NF as the substrate is directly etched in acidic ferric nitrate solution and forms lots of holes.

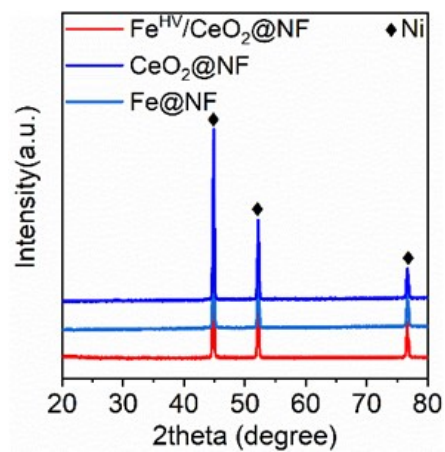


Fig. S7 XRD patterns of $\text{Fe}^{\text{HV}}/\text{CeO}_2@\text{NF}$ and $\text{CeO}_2@\text{NF}$. The XRD patterns of the samples are shown in Fig. S7. Only the peaks of Ni ascribed to the nickel foam substrate are observed, and no peaks of FeO_x are detected. This is probably due to the uniform distribution (Fig. 1b) and the ultra-small size (less than 5 nm) of FeO_x nanoparticles.

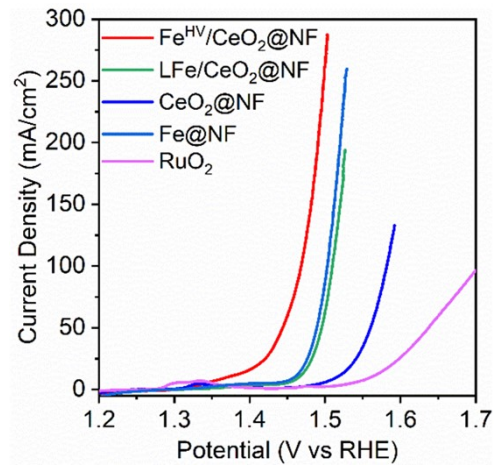


Fig. S8 Polarization curves of Fe^{HV}/CeO₂@NF and reference catalysts with a scan rate of 10 mV/s.

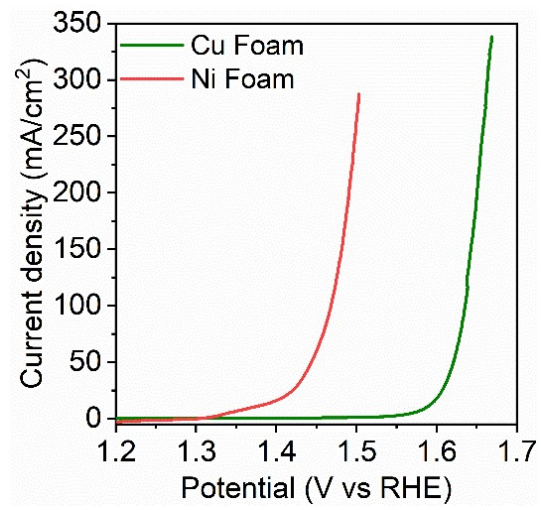


Fig. S9 The polarization curves with Ni foam and Cu foam substrate.

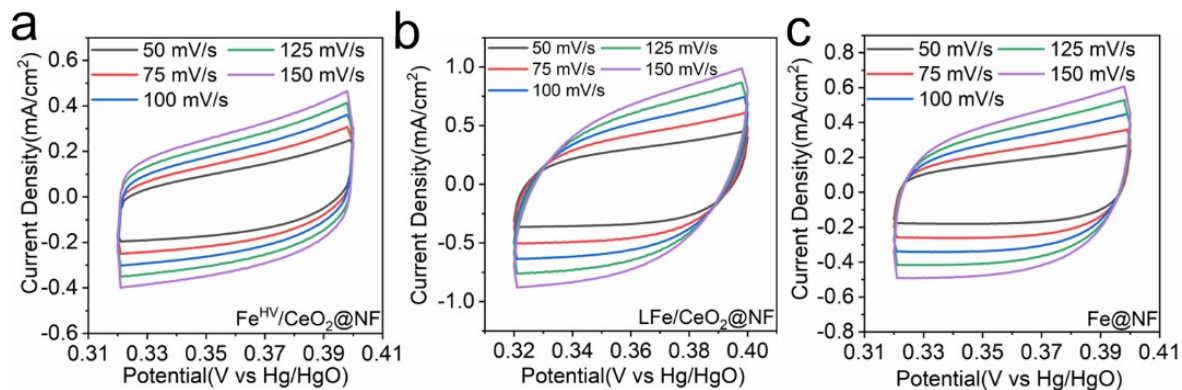


Fig. S10 Cyclic voltammetry curves of (a) $\text{Fe}^{\text{HV}}/\text{CeO}_2@\text{NF}$ (b) $\text{LFe}/\text{CeO}_2@\text{NF}$ and (c) $\text{Fe}@\text{NF}$ catalysts. The cyclic voltammetry (CV) was tested on $\text{Fe}^{\text{HV}}/\text{CeO}_2@\text{NF}$, $\text{Fe}@\text{NF}$ and $\text{LFe}/\text{CeO}_2@\text{NF}$ catalysts in the non-Faraday potential range (0.32-0.40 V vs Hg/HgO) and calculated the electrochemical double-layer capacitance (C_{dl}) of the three catalysts. The ECSA was calculated according to the formula $\text{ECSA} = C_{\text{DL}} / C_{\text{S}}$, where a specific capacitance of $C_{\text{S}} = 0.040 \text{ mF}/\text{cm}^2$ was used in this work.

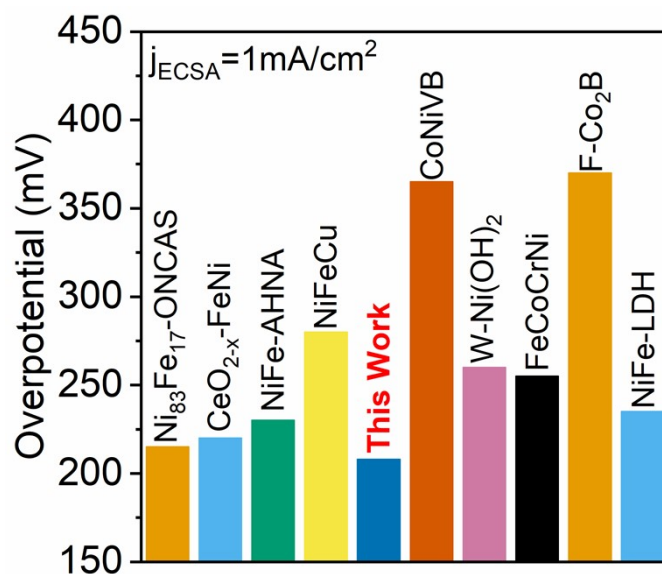


Fig. S11 Comparison of intrinsic activity of OER electrocatalysts. This was obtained by comparing the overpotential at an ECSA normalized current density of 1 mA/cm². The result shows that the Fe^{HV}/CeO₂@NF catalyst has the best OER specific activity among these catalysts.

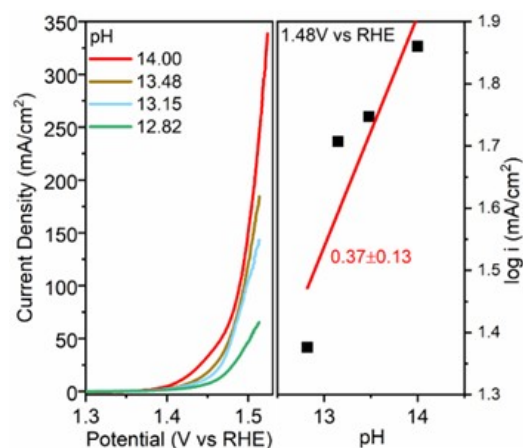


Fig. S12 LSV curves of $\text{Fe}^{\text{HV}}/\text{CeO}_2@\text{NF}$ in KOH with different pH value (left) and the OER current density at 1.48 V versus RHE plotted in log scale as a function of pH, from which the proton reaction orders ($\rho_{\text{RHE}} = \partial \log i / \partial \text{pH}$) were calculated (right). The OER activities of $\text{Fe}^{\text{HV}}/\text{CeO}_2@\text{NF}$ was assessed at different pH conditions (pH = 14, 13.48, 13.15, 12.82). The result shows the OER current density at 1.48 V (vs. RHE) in log scale as a function of pH, from which the proton reaction orders on RHE scale ($\rho_{\text{RHE}} = \partial \log i / \partial \text{pH}$) are calculated to be 0.37. The small ρ_{RHE} for $\text{Fe}^{\text{HV}}/\text{CeO}_2@\text{NF}$ implies a weak pH-dependent OER activity, which indicates that the adsorption mechanism is still dominant.

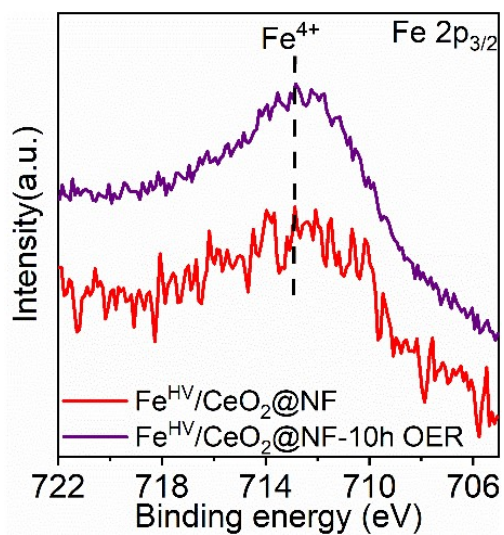


Fig. S13 Fe 2p XPS spectra of the Fe^{HV}/CeO₂@NF catalyst before and after 10-hour OER test at the current density of 30 mA/cm². The 2p_{3/2} peak still locates at about 713 eV corresponding to Fe⁴⁺, which proves the excellent stability of Fe⁴⁺ in the Fe^{HV}/CeO₂@NF catalyst.

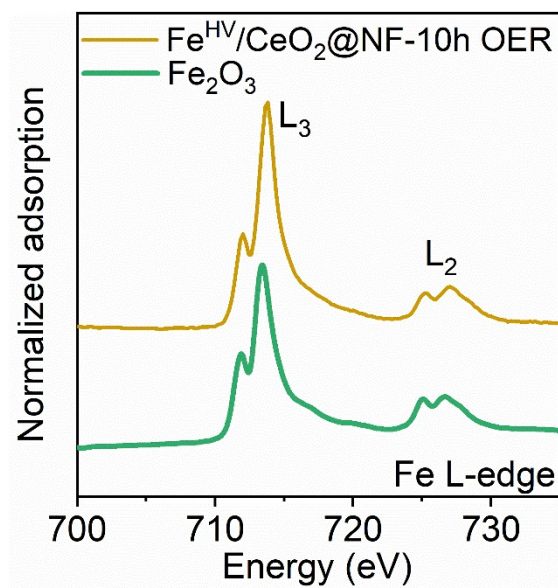


Fig. S14 The soft X-ray absorption spectroscopy of Fe L-edge of the $\text{Fe}^{\text{HV}}/\text{CeO}_2/\text{NF}$ catalyst after 10-hour OER test at the current density of 30 mA/cm^2 . Compared with standard Fe_2O_3 , the Fe L-edge in $\text{Fe}^{\text{HV}}/\text{CeO}_2/\text{NF}$ -10h OER presents a blue shift, which suggests a higher Fe valence state than +3 in Fe_2O_3 .

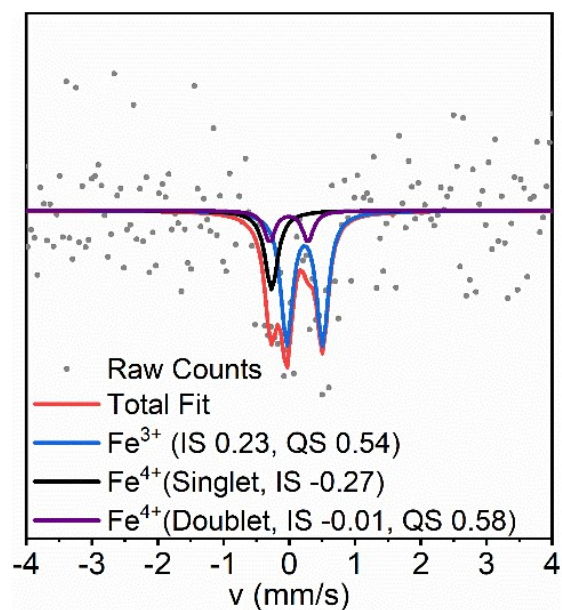


Fig. S15 Fe Mössbauer spectrum of the Fe^{HV}/CeO₂@NF catalyst after 10-hour OER test at the current density of 30 mA/cm². The overall fitting curve as well as the curves of its components are also shown. The result revealed a doublet with an isomer shift (IS, ν) of 0.23 mm/s and quadrupole splitting (QS, Δ) of 0.54 mm/s corresponding to Fe³⁺. A shoulder at $\nu = -0.27$ mm/s and a doublet at $\nu = -0.01$ mm/s corresponding to Fe⁴⁺ appeared. The excellent stability of Fe⁴⁺ in the Fe^{HV}/CeO₂@NF catalyst is proved.

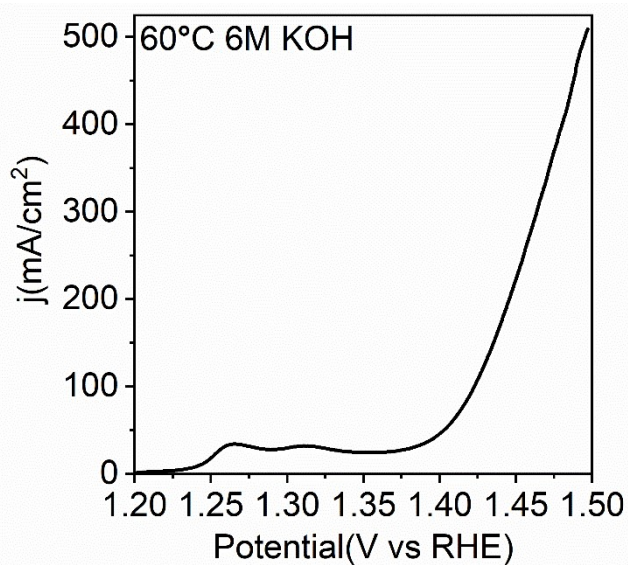


Fig. S16 LSV curve of the Fe^{HV}/CeO₂@NF catalyst. (6 M KOH and 60°C). The polarization curve shows the current density can reach 500 mA/cm² at the overpotential of 270 mV (without iR compensation).

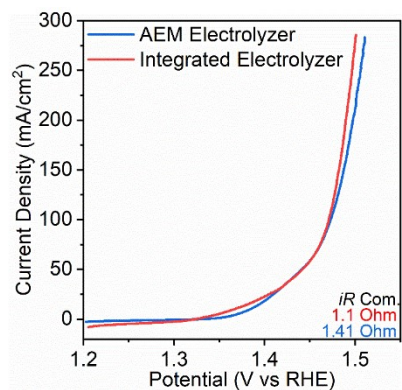


Fig. S17 The polarization curves of Fe^{HV}/CeO₂@NF measured in AEM and Integrated Electrolyzer. The OER activity of Fe^{HV}/CeO₂@NF was also performed in the lab-scale anion exchange membrane electrolyzer. After iR compensation, the OER performances of Fe^{HV}/CeO₂@NF are nearly the same in AEM and Integrated electrolyzer. This indicates the Fe^{HV}/CeO₂@NF catalyst is promising to be used for industry water splitting.

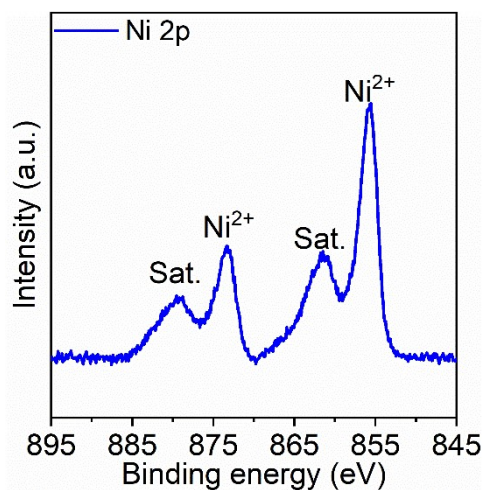


Fig. S18 Ni 2p XPS of $\text{Fe}^{\text{HV}}/\text{CeO}_2@\text{NF}$ catalyst after 10-hour OER test at the current density of $30 \text{ mA}/\text{cm}^2$. The typical Ni 2p peaks at 873.3 eV and 855.7 eV ascribed to Ni^{2+} are observed obviously for $\text{Fe}^{\text{HV}}/\text{CeO}_2@\text{NF}$ after 10-hour OER test, indicating the NiFe oxide has formed during the OER reaction (Adv. Funct. Mater. 2020, 30, 1908367).

Tables

Table S1. The activity comparison of OER catalysts. This was obtained by comparing the overpotential to reach the geometric current density of 30, 50, and 100 mA/cm² among Fe^{HV}/CeO₂@NF catalyst and recently reported OER catalysts, indicating the indeed excellent OER activity of the Fe^{HV}/CeO₂@NF catalyst.

Catalyst	Electrolyte	Overpotential (mV)			Reference
		30 mA/cm ²	50 mA/cm ²	100 mA/cm ²	
Fe^{HV}/CeO₂@NF	1.0 M KOH	210	219	238	This work
NiFeCu	1.0 M KOH	200	220	260	6
Ni ₈₃ Fe ₁₇ -ONCAS	1.0 M KOH	200	220	230	7
NiFe-LDH	1.0 M KOH	230	230	/	8
ZnCoOOH	1.0 M KOH	250	250	290	9
FeCoCrNi	1.0 M KOH	230	245	260	10
CoFeAlO	1.0 M KOH	300	310	330	11
CeO _{2-x} -FeNi	1.0 M KOH	220	245	270	12
FeOOH/CeO ₂	1.0 M NaOH	250	270	310	13
S-NiN	1.0 M KOH	300	315	330	14

Table S2. Electrochemistry parameters of catalysts investigated in 1 M KOH.

Catalyst	C _{DL} (mF/cm ²)	ECSA (cm ²)	Tafel slope (mV/decade)
Fe@NF	3.73	93	62
Fe ^{HV} /CeO ₂ @NF	1.68	42	40
LFe/CeO ₂ @NF	8.37	209	79

Table S3. Comparison of specific activity between Fe^{HV}/CeO₂@NF catalyst and a series of recently reported high OER performance catalysts. This is acquired by comparing the overpotential at an ECSA normalized current density of 1 mA/cm². The result shows that the Fe^{HV}/CeO₂@NF catalyst has the best OER specific activity among these catalysts.

Catalysts	Electrolyte	C _{dl} (mF/cm ²)	Cs (μF/cm ²)	η (mV)	Reference
Fe^{HV}/CeO₂@NF	1.0 M KOH	1.68	40	208	This work
Ni₈₃Fe₁₇-ONCAS	1.0 M KOH	2.26	40	215	7
CeO_{2-x}-FeNi	1.0 M KOH	0.75	40	220	12
NiFe-AHNA	1.0 M KOH	3.2	40	230	15
NiFeCu	1.0 M KOH	54.24	40	280	6
CoNiVB	1.0 M KOH	1.01	40	365	16
W-Ni(OH)₂	1.0 M KOH	2	/	260	17
FeCoCrNi	1.0 M KOH	2.7	40	255	10
F-Co₂B	1.0 M KOH	53.84	40	370	18
H-NiFe-LDH	1.0 M KOH	7.22	/	235	8

Table S4. Stability comparison of recently reported efficient OER electrocatalysts (The electrolyte is 1 M KOH or NaOH). This table summarizes the stability comparison of recently reported efficient oxygen evolution catalysts and the Fe^{HV}/CeO₂@NF catalyst, and shows that the stability of Fe^{HV}/CeO₂@NF is outstanding among them. Degradation evaluation: the increase in overpotential or decrease in current density between the beginning and the end of the stability test.

Catalysts	Current density (mA/cm ²)	Overpotential (mV)	Time (h)	Degradation	Reference
FeCoCrNi	10	304	20	-1 mA/cm ²	10
CeO _{2-x} -FeNi	10	195	48	+20 mV	12
NiCeO _x	10	300	200	-20 mV	19
MoO ₂ -Ni	10	250	480	+30 mV	20
(Co _{1-x} Ni _x)(S _{1-y} P _y) ₂ /G	10	300	100	+10 mV	21
UfD-RuO ₂ /CC	10	210	20	+19 mV	22
Ag@Co-LDH	10	230	50	+10 mV	23
HCM@Ni-N	20	380	12	+19 mV	24
ZnCoOOH	20	245	40	+10 mV	9
NiFeB-P	50	560	23	+5 mV	25
NiFe-PBA/Ni ₃ C(B)	100	250	22	-20 mA/cm ²	26
W-Ni(OH) ₂	100	260	3	/	17
S-NiN	100	350	10	+10 mV	14
Fe^{HV}/CeO₂@NF	200	296	500	+16 mV	This work
NiFe/Co ₃ O ₄ @NF	200	290	24	-9 mA/cm ²	27
NiFeCu	200	325	6	+10 mV	6
FeOOH/CeO ₂	200	400	50	-10 mA/cm ²	13
Ni ₈₃ Fe ₁₇ -ONCAS	200	300	120	+30 mV	7
EP NiFeCo-CST	1000	260	100	+20 mV	28

Supplementary References

1. S. J. Clark, M. D. Segall, C. J. Pickard, P. J. Hasnip, M. I. J. Probert, K. Refson, M. C. Payne, *Zeitschrift Fur Kristallographie*, 2005, **220**, 567-570.
2. Perdew, Burke, Ernzerhof, *Phys. Rev. Lett.*, 1997, **77**, 3865-3868.
3. P. J. Hasnip, C. J. Pickard, *Comput Phys Comm.*, 2006**174**, 24-29.
4. Perdew, Chevary, Vosko, Jackson, Pederson, Singh, Fiolhais, *Physical Review B*, 1992, **46**, 6671-6687.
5. J. D. Head, M. C. Zerner, *Chem Phys Lett.*, 1985, **122**, 264-270.
6. P. Zhang, L. Li, D. Nordlund, H. Chen, L. Fan, B. Zhang, X. Sheng, Q. Daniel, L. Sun, *Nat. Comm.*, 2018, **9**, 381.
7. P. Liu, B. Chen, C. Liang, W. Yao, Y. Cui, S. Hu, P. Zou, H. Zhang, H. J. Fan, C. Yang, *Adv. Mater.*, 2021, **33**, 2007377.
8. Z. Qiu, C. W. Tai, G. A. Niklasson, T. Edvinsson, *Energy Environ. Sci.*, 2019, **12**, 572.
9. Z. F. Huang, J. Song, Y. Du, S. Xi, S. Dou, J. M. V. Nsanzimana, C. Wang, Z. J. Xu, X. Wang, *Nat. Energy*, 2019, **4**, 329-338.
10. N. Zhang, X. Feng, D. Rao, X. Deng, L. Cai, B. Qiu, R. Long, Y. Xiong, Y. Lu, Y. Chai, *Nat. Comm.*, 2020, **11**, 4066.
11. T. Wu, S. Sun, J. Song, S. Xi, Y. Du, B. Chen, W. A. Sasangka, H. Liao, C. L. Gan, G. G. Scherer, L. Zeng, H. Wang, H. Li, A. Grimaud, Z. J. Xu, *Nature Cataly.*, 2019, **2**, 763-772.
12. J. Yu, J. Wang, X. Long, L. Chen, Q. Cao, J. Wang, C. Qiu, J. Lim, S. Yang, *Adv. Energy Mater.*, 2021, **11**, 2002731.
13. J. X. Feng, S. H. Ye, H. Xu, Y. X. Tong, G. R. Li, *Adv. Mater.*, 2016, **28**, 4698-4703.
14. Y. Hou, M. Qiu, M. G. Kim, P. Liu, G. Nam, T. Zhang, X. Zhuang, B. Yang, J. Cho, M. Chen, C. Yuan, L. Lei, X. Feng, *Nat. Comm.* 2019, **10**, 1392.
15. C. Liang, P. Zou, A. Nairan, Y. Zhang, J. Liu, K. Liu, S. Hu, F. Kang, H. J. Fan, C. Yang, *Energy Environ. Sci.*, 2020, **13**, 86.

16. H. Han, Y. R. Hong, J. Woo, S. Mhin, K. M. Kim, J. Kwon, H. Choi, Y. C. Chung, T. Song, *Adv. Energy Mater.*, 2019, **9**, 1803799.
17. J. Yan, L. Kong, Y. Ji, J. White, Y. Li, J. Zhang, P. An, S. Liu, S. T. Lee, T. Ma, *Nat. Comm.*, 2019, **10**, 2149.
18. H. Han, H. Choi, S. Mhin, Y. R. Hong, K. M. K, J. Kwon, G. Ali, K. Y. Chung, M. Je, H. N. Umh, D. H. Lim, K. Davey, S. Z. Qiao, U. Paik, T. Song, *Energy Environ. Sci.* 2019, **12**, 2443.
19. J. Yu, Q. Cao, Y. Li, X. Long, S. Yang, J. K. Clark, M. Nakabayashi, N. Shibata, J. J. Delaunay, *ACS Catal.*, 2019, **9**, 1605-1611.
20. X. Liu, J. Meng, K. Ni, R. Guo, F. Xia, J. Xie, X. Li, B. Wen, P. Wu, M. Li, J. Wu, X. Wu, L. Mai, D. Zhao, *Cell Reports Phy. Sci.*, 2020, **1**, 100241.
21. H. J. Song, H. Yoon, B. Ju, G. H. Lee, D. W. Kim, *Adv. Energy Mater.*, 2018, **8**, 1802319.
22. R. Ge, L. Li, J. S, Y. Lin, Z. Tian, L. Chen, *Adv. Energy Mater.*, 2019, **9**, 1901313.
23. M. Zhang, Y. Zhang, L. Ye, B. Guo, Y. Gong, *App. Catal. B: Environ.*, 2021, **298**, 120601.
24. H. Zhang, Y. Liu, T. Chen, J. Zhang, J. Zhang, X. W. D. Lou, *Adv. Mater.*, 2019, **31**, 1904548.
25. Y. Kang, Y. Guo, J. Zhao, B. Jiang, J. Guo, Y. Tang, H. Li, V. Malgras, M. A. Amin, H. Nara, Y. Sugahara, Y. Yamauchi, T. Asahi, *Small*, 2022, **18**, 2203411.
26. X. Lin, S. Cao, H. Chen, X. Chen, Z. Wang, S. Zhou, H. Xu, S. Liu, S. Wei, X. Lu, *Chem. Eng. Journal*, 2022, **433**, 133524.
27. J. Lv, L. Wang, R. Li, K. Zhang, D. Zhao, Y. Li, X. Li, X. Huang, G. Wang, *ACS Catal.*, 2021, **11**, 14338–14351.
28. J. Mo, Y. Ko, Y. S. Yun, J. Huh, J. Cho, *Energy Environ. Sci.*, 2022, **15**, 3815-3829.